

# Comet 62P/Tsuchinshan 1: A photometric investigation of an evolving dust production rate and other cometary properties at small heliocentric distances post-perihelion

DARAGH M. HOLLMAN<sup>1</sup>

<sup>1</sup>*School of Physics, University College Dublin, Ireland*

## ABSTRACT

We presented photometric observations with Johnson-Cousins filters of comet 62P/Tsuchinshan 1 taken in March 2024. The dust rate proxy was determined for the standard reference aperture radius  $\rho = 10^4$  km, and was phase corrected to  $0^\circ$  to yield an average R band  $Af\rho = (73 \pm 21)$  cm, B band  $Af\rho = (59 \pm 5)$  cm, and V band  $Af\rho = (70 \pm 14)$  cm. We found absolute magnitudes in the B, V, and R bands of  $14.34 \pm 0.16$ ,  $13.95 \pm 0.23$ , and  $13.59 \pm 0.22$  respectively, measured with a photometric aperture radius  $\rho = 10^4$  km. Dust colours were subsequently determined with colour indices  $B - V = 0.45 \pm 0.3$  and  $V - R = 0.3 \pm 0.4$  with reddening =  $(0.9 \pm 2.7)$  % per  $1000 \text{ \AA}$  between the B and V filters, and reddening =  $(2 \pm 4)$  % per  $1000 \text{ \AA}$  between the V and R filters, through which the presence of gas emission was inferred. Dramatic short term variations in the dust colour were observed and attributed to a heterogeneous chemical composition of the nucleus. An upper limit to the nucleus radius was determined through a coma correction method and found to be  $r_{\text{nucleus}} \leq 5.48$  km.

*Keywords:* Comets, 62P/Tsuchinshan 1, Photometry, Activity, Dust Colour, Nucleus Radius

## 1. INTRODUCTION

Comets are considered to be remnants of the protostellar disc from which the solar system formed (Mazzotta Epifani et al. 2007). Since then, many have been swept up to become part of the giant planets, or gravitationally perturbed to become part of the Oort Cloud or Kuiper Belt, or even ejected from the Solar System entirely (Cochran et al. 2015). What remains spends much of its time far from the sun, in the coldest regions of the planetary system, undergoing little change from their original states at the time of the formation of the Solar System (Mazzotta Epifani et al. 2007; Cochran et al. 2015). Comets were formed over a wide range of distances and conditions which give way to the diverse range of comets observed to date (Cochran et al. 2015). For this reason, comets are important objects to study, as their collective behaviour can better constrain models of the early solar nebula (Cochran et al. 2015).

Comets can be thought of as “dirty snowballs” due to their composition of ices and dust (Cochran et al. 2015). As a comet approaches the sun along its orbit and begins to heat up, these ices start to sublimate. Comets are typically small, and due to an insufficiently strong gravitational force, the gas expands outwards from the surface (Cochran et al. 2015). This sublimating gas carries with it some of the solid particles of the comet (dust and ice grains, and their aggregates) (Cochran et al. 2015). The emission of this material over time forms the coma, a cloud of dust and ice grains surrounding the nucleus. At small heliocentric distances,

this becomes so prominent that the nucleus itself is often not observable (Cochran et al. 2015). The dust in the coma stretches out behind the comet as it is pushed away by the solar wind, which forms a tail in the wake of the comet’s motion. As the same comet passes perihelion it will subsequently cool down and the coma will decrease in size. The measure of the production rate of dust from the nucleus to the coma is referred to as the activity of the comet, and is typically quantified with the dust rate proxy  $Af\rho$ , as expanded upon in later sections (Garcia & Gil-Hutton 2021; A’Hearn et al. 1984).

The colour of the coma is determined by the scattering of light from the sun off grains of dust. Grains smaller than the wavelength of the light scatter more towards the blue and larger grains scatter neutrally or more towards the red (Meech et al. 2009). Typical comet compositions result in predominantly redder colours (Bauer et al. 2022). We don’t expect the colour of the coma to change with heliocentric distance (Bauer et al. 2022; Meech et al. 2009). However, at small distances the composition of the comet can play a role in the colour. When near the sun, comets typically have strong emission from gas species in the coma, biasing the coma colours towards the blue, the strength of which typically varies with  $r^{-2}$  (Meech et al. 2009; Ivanova et al. 2014). Far from the sun, the colour should only vary with the properties of the dust grains (Meech et al. 2009; Kolokolova et al. 2004). The total scattered light is thereby a function comprising the scattering of a distribution of irregularly shaped particles with differing

compositions and sizes (Meech et al. 2009). Grain properties can be determined from colour data through the use of complex models as shown by Korsun & Chörny (2003). The application of such models are however outside the scope of this study.

Short period comet 62P/Tsuchinshan 1 (further referred to as 62P) has been observed in the past both near aphelion (in 2006) (Fernández et al. 2013) and near perihelion (Jehin et al. 2023, 2024a,b; Li et al. 2023). In this study we present further photometric observations of 62P at small heliocentric distances post perihelion, along with analysis of the activity, dust colour, and the inference of an upper limit to the radius of the nucleus. Section 2 describes in detail the observations made of 62P along with the image reduction and pre-processing steps. It also outlines in detail the analysis steps taken to determine the dust rate proxy,  $Af\rho$ , along with dust colours and derived quantities, and estimating the nucleus radius for active comets. Section 3 presents all results of these analyses and discusses the results with reference to past observations of 62P and other short period comets. Finally, section 4 concludes by summarising the new findings of 62P, and placing them in the context of previous observations of 62P and other comets.

## 2. OBSERVATIONS AND ANALYSIS

62P was chosen as the target of this study for several reasons, including but not limited to: a small heliocentric distance, a bright visual magnitude, a small proper motion, and a low phase angle. Observations took place over four days across four fields, yielding 87 CCD images of 120 seconds exposure for a total observation time of 10.44 ks. The 1.23 m telescope at the Calar Alto Observatory in Andalusia, Spain with a CCD detector of  $4096 \times 4108$  square pixels of  $15 \mu\text{m}$  was used for all observations.  $2 \times 2$  binning was utilised to reduce readout time. Johnson-Cousins broadband filters B, V, and R were used equally in the observations. Full details of the observations and corresponding ephemeris information can be found in tables 1 and 2 respectively.

### 2.1. Image Reduction and Pre-Processing

Each image was reduced using bias, dark, and flat field images. 21 bias images, 21 darks, and 5 flats in each filter were taken, all of which were median stacked to create “master” images. The master flats were normalised by dividing each pixel by the maximum value in the image. All images were calibrated by subtracting

the master bias and dark (also bias subtracted) from the image and subsequently dividing by the normalised master flat.

The images were aligned to the comet photocentre before coadding (Mazzotta Epifani et al. 2007, 2010; Garcia & Gil-Hutton 2021; Meech et al. 2009). In this study, the Python package PHOTUTILS (Bradley et al. 2023) - specifically the source detection function *DAOSTarFinder* - was used to find the photocentre. While this function is traditionally used to find stars, it also proves effective for finding the comet in successive frames (as the centre of the comet will look like a point source). Given some constraints on maximum counts and distance from a rough position, a simple algorithm was used to differentiate the comet from the other sources in each successive image. These were then cropped to align the source centre to a specific position in the image. These resulting images were then coadded using median stacking to ensure anomalies were ignored (such as cosmic rays or satellites), and to reduce the brightness of the background stars. Stacked comet images for observations on 2024-03-13 can be found in figure 1, and stacked images for all observations can be found in appendix A. Each set of observation images were also stacked aligning the stars, in order to maximise the signal-to-noise of reference stars for determining quantities such as the zeropoint.

#### 2.1.1. Star Removal

In addition to median stacking, further steps were taken to isolate the comet from the background sky. A method was employed to replace the stars with their surrounding signal, reducing their contribution to the image. PHOTUTILS source detection methods were used to locate the stars. A circular aperture of  $10''$  radius was centred on each star and replaced with the average flux of a surrounding annulus of inner radius  $12''$  and outer radius  $18''$ . The effectiveness of this method was very dependent on the choice of these annulus radii, and values could be chosen to almost completely remove the stars from the images. However, due to some stars being within, or near to the coma, any adjustments made on these stars would distort the coma signal inducing non-physical artifacts. Hence, these radii values were chosen to maximise the removal of stars in the image, whilst minimising the creation of artifacts in the coma.

#### 2.1.2. Photometry

The comet fluxes in each stacked image were determined using circular aperture photometry with PHOTU-

Date	UT (start)	R.A.	DEC	$R_h$ [au]	$\Delta$ [au]	Phase [°]	Filters	Exp (s)	No. Images
2024-03-13	01:40:42	12 27 52	10 15 40	1.566	0.585	9.62	BVR	120	21
2024-03-14	03:46:47	12 26 44	10 15 24	1.573	0.591	9.15	BVR	120	12
2024-03-15	01:57:17	12 25 44	10 14 56	1.579	0.595	8.64	BVR	120	21
2024-03-18	01:54:17	12 21 54	10 20 28	1.599	0.612	7.52	BVR	120	33

**Table 1. Observing Conditions:** Observational circumstances per day. The UT time marks the start time of each sequence of observations, with each set a programmed sequence for an observing time of  $\text{Exp} \times \text{No. Images}$  (excluding readout time and filter changes) for each night. The number of observations on each night was constrained by weather conditions, resulting in a shortened observation on 2024-03-14 but also a lengthened observation on 2024-03-18.  $R_h$  is the heliocentric distance of 62P,  $\Delta$  is the geocentric distance of 62P, "Exp" is the length of each exposure, and "No. Images" is the number of observations taken in the sequence.

Comet	a [au]	q [au]	e	P [years]	peri [°]	Node [°]	i [°]
62P/Tsuchinshan 1	3.37	1.26	0.624	6.19	47.3	68.67	4.74

**Table 2. Ephemeris:** Orbital information for 62P. From left to right, the fields are: semimajor axis, perihelion distance, orbital eccentricity, orbital period, argument of the perifocus, longitude of the ascending node, and inclination. These data - corresponding to the first observation date and time (2024-03-13, 01:40:42) - were retrieved from JPL's Horizons System (Giorgini et al. 1996) on 2024-04-15.

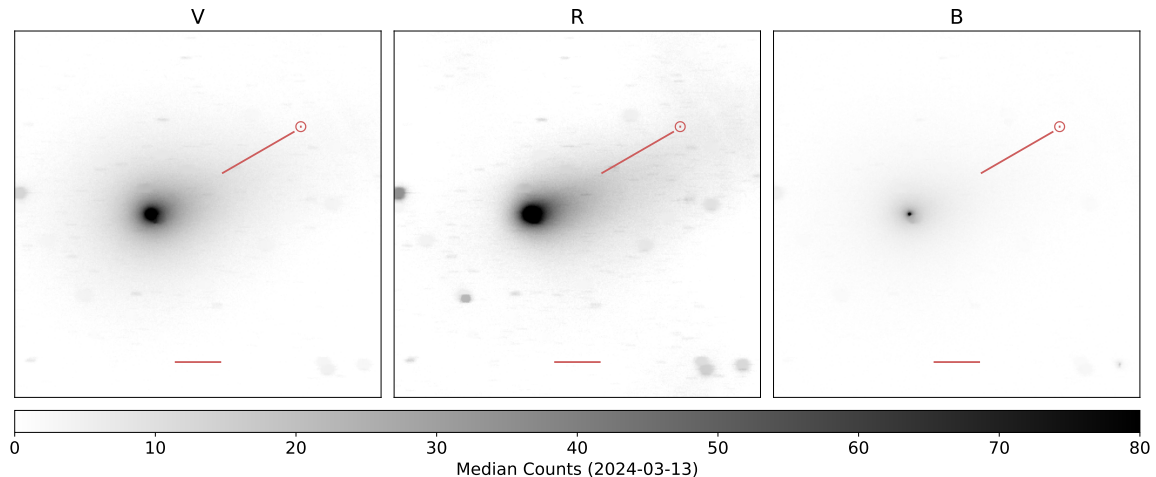


**Figure 1. Image Stacking:** Coadded images for observations on 2024-03-13 for each photometric filter. In each image, north is vertically upwards, and east to the left. It's clear that the star removal techniques employed were not entirely effective as some bright stars are still visible in the image as smudges. The position angle vector to the sun is indicated by a diagonal red line pointing to the symbol:  $\odot$ . Scale is marked by the horizontal red line which is of length 50,000 km. We saturate the colourmap at 80 counts to better show the extent of the coma and tail. The same colourmap was applied to each image to highlight the differences between photometric filters. We see the tail of the comet much clearer in the R band, whilst the coma and tail are comparatively negligible in the B band.

TILS. The sky background was determined using sigma clipped statistics (routines from the Python package *ASTROPY* (Astropy Collaboration et al. 2022)) to find the median background whilst rejecting counts below 5 standard deviations. The median background was subtracted from each image before stacking to ensure the stacked images (both aligned to the comet and to stars) were also without background signal. Magnitudes for a given flux within an aperture were calculated in the

standard method, with zeropoint calibration determined from the comparison of three background reference stars (far from the coma) with the APASS (data release 9) catalog (Henden et al. 2016). Zeropoint was determined for all three photometric filters. This catalogue had Johnsons-Cousins B and V band magnitudes for all reference stars, but R band magnitudes needed to be determined with conversions from Sloan  $r'$  and  $i'$  band

magnitudes by [Jordi et al. \(2006\)](#).

### 2.1.3. Dust Production

A proxy for the dust production rate (also referred to as activity),  $Af\rho$ , was introduced by [A’Hearn et al. \(1984\)](#) to enable the comparison of cometary activity irrespective of observing conditions. The parameter can be derived in terms of the difference between the total magnitude of the comet and the solar magnitude in the same band as follows ([Mazzotta Epifani et al. 2007](#)):

$$Af\rho = \frac{4R_h^2\Delta^2}{\rho} 10^{0.4(m_\odot - m_{\text{total}})} \quad (1)$$

where  $m_\odot$  is the solar magnitude,  $m_{\text{total}}$  is the comet total magnitude at aperture radius  $\rho$ .  $r_h$  is the heliocentric distance and  $\Delta$  is the geocentric distance (in au and km respectively) ([Garcia & Gil-Hutton 2021](#); [Mazzotta Epifani et al. 2007](#)). As  $Af\rho$  changes with aperture radius  $\rho$ , the proxy was calculated over a large range of radii, with reference values subsequently taken for the standard reference aperture of  $\rho = 10^4$  km. The Python package SBPY - “Python for Small Bodies” ([Mommert et al. 2019](#)) - specifically the submodule ACTIVITY, was used to determine the  $Af\rho$  parameter. This package was also used to correct the proxy to what it would be measured as at a zero phase angle. SBPY uses the Halley-Marcus composite phase function by [Schleicher \(2010\)](#). The phase angle of the comet (i.e. the angle spanning the sun-target-observer) was retrieved using JPL’s Horizons System ([Giorgini et al. 1996](#)).

### 2.1.4. Dust Colour

The total magnitude of the comet in each photometric filter was determined at the reference aperture  $\rho = 10^4$  km as discussed above. Colour indices  $B - V$  and  $V - R$  were calculated for each day of observations. Dust colour indices can be further used to derive dust reddening, the percentage change in the strength of the continuum per 1000 Å ([Mazzotta Epifani et al. 2010](#); [Lara et al. 2003](#)). Reddening can be derived in terms of activity measurements with the following relation:

$$\text{reddening} = \frac{1}{(Af\rho)} \frac{(Af\rho)' - (Af\rho)}{\lambda' - \lambda} \quad (2)$$

where the activity in different photometric filters is used to describe the difference in colour ([Mazzotta Epifani et al. 2010](#)).  $Af\rho$  values for the reference aperture  $\rho = 10^4$  km were used in this calculation to determine reddening for both  $B - V$  and  $V - R$   $Af\rho$  values.

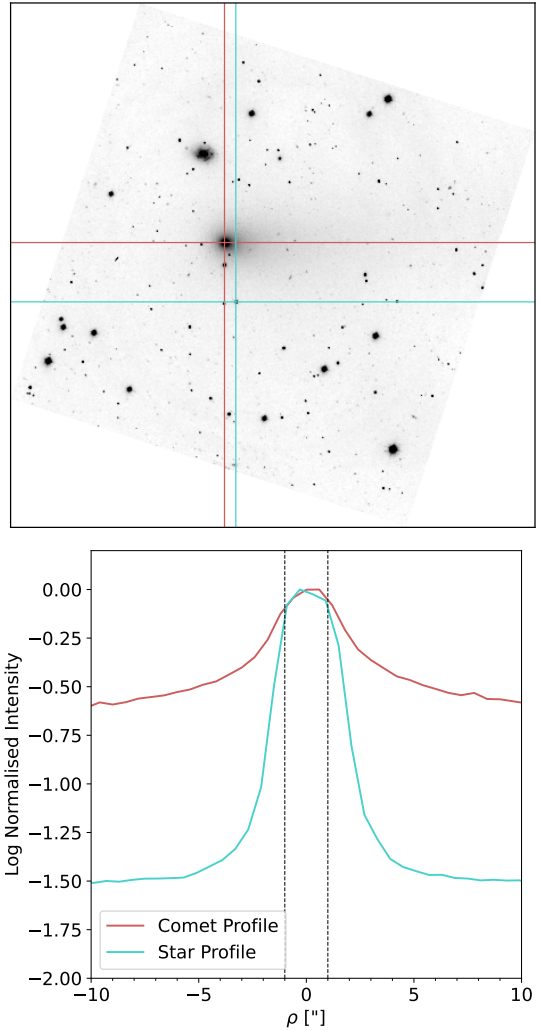


**Figure 2. Comet-Star Profile Comparison:** *Upper Panel:* The image with the best seeing (2024-03-14 in R) was chosen and rotated by  $18^\circ$  to align the tail of the comet horizontally. A vertical profile was then taken perpendicular to the tail to remove asymmetries. The lines correspond to the horizontal and vertical profiles of the comet, whilst blue lines correspond to a nearby field star to compare with. *Lower Panel:* The comet profile (red) compared with the profile of a nearby field star (blue). We see the profile of the comet behaves as a point source up to  $\approx 1''$  and hence, the relative signal increase outside of this must be due to the coma. This is a very small portion of the profile, and hence there must be a large contamination to the nucleus magnitude from the coma.

### 2.1.5. Nucleus Radius

As 62P was highly active at the time of observations with a large coma, standard methods of determining the size of the comet are not directly applicable given the bare nucleus was not observed in isolation. Following a method outlined by [O’Ceallaigh et al. \(1995\)](#) (and typ-

ically used for active comets (Mazzotta Epifani et al. 2007; Lowry & Fitzsimmons 2001), an upper limit for the radius of the nucleus was determined as follows: To determine if the bare nucleus was observed, the profile of the comet was compared to that of a nearby field star. This was done for the image where the seeing was the best (FWHM 1.5"). To avoid asymmetries in the profile, the image was first rotated such that the tail of the comet was aligned perpendicular to the profile. Figure 2 shows the resulting normalised log intensity profiles of 62P and a nearby field star. We see the comet profile follows the star profile up to approximately 1" from the centre after which an excess is present in the comet profile. O’Ceallaigh et al. (1995) interpret this excess as a contamination from the coma, and suggest subtracting the coma magnitude from the total magnitude to find the nucleus magnitude. The "coma contamination" was determined with the relation by Jewitt (1991) for steady state comae:

$$m_{\text{coma}} = \Sigma_{\lambda}(\rho) - 2.5 \log_{10}(2\pi\rho^2) \quad (3)$$

with a given surface brightness profile  $\Sigma_{\lambda}(\rho)$ . The choice of aperture for this calculation was outlined in detail in appendix B. The approximation of a steady state coma is somewhat questionable, but gives a good estimate of the coma contamination to the nucleus (Mazzotta Epifani et al. 2007). By making use of the difference of magnitudes we can find the contribution of the coma flux to the total flux:

$$\frac{F_{\text{coma}}}{F_{\text{total}}} = 10^{-0.4(m_{\text{coma}} - m_{\text{total}})} \quad (4)$$

and similarly:

$$\frac{F_{\text{nucleus}}}{F_{\text{total}}} = 1 - \frac{F_{\text{coma}}}{F_{\text{total}}} = 10^{0.4(m_{\text{nucleus}} - m_{\text{total}})} \quad (5)$$

from which the magnitude of the nucleus can be derived in terms of the total magnitude and the coma contamination (Mazzotta Epifani et al. 2007).

$$m_{\text{nucleus}} = m_{\text{total}} - 2.5 \log_{10} \left( 1 - \frac{F_{\text{coma}}}{F_{\text{total}}} \right) \quad (6)$$

The nucleus magnitude was then be reformulated to determine the radius of a spherical object (Jewitt 1991; Mazzotta Epifani et al. 2007):

$$Ar_{\text{nucleus}}^2 = 2.24 \times 10^{22} R_h^2 \Delta^2 10^{0.4(m_{\odot} - m_{\text{nucleus}} + \beta\alpha)} \quad (7)$$

where  $A$  is the geometric albedo,  $r_{\text{nucleus}}$  is the radius of the target in metres,  $m_{\odot}$  is the magnitude of the sun in the same filter as the observations, and  $\alpha$  and  $\beta$  are the phase angle and phase coefficient respectively. For

active comets - as is the case for these observations of 62P - equation 7 can only be used as an upper limit of the radius (Mazzotta Epifani et al. 2007). In this study, as there is no data over a range of phase angles, we assume the common value of  $\beta = 0.035 \text{ mag deg}^{-1}$  (Lamy et al. 2004; Mazzotta Epifani et al. 2007). The albedo of  $A = 0.04$  is typically assumed for a cometary nucleus (Mazzotta Epifani et al. 2007). Values have been measured commonly between  $A = 0.02$  and  $A = 0.06$  (A’Hearn et al. 1989; Lamy et al. 2004), and higher values are possible (Bus et al. 1989; Cruikshank & Brown 1983). Hence, a "radius curve", plotting nuclear radius as a function of albedo, is appropriate (Mazzotta Epifani et al. 2007).

### 3. RESULTS AND DISCUSSION

#### 3.1. Activity

For each night of observations, the magnitude of 62P and corresponding phase corrected  $Af\rho$  were determined in each filter for the standard reference aperture of  $10^4 \text{ km}$ , see table 3. A weighted mean was determined for each of the parameters to give an average behaviour over the time observed. The uncertainties on the data of each day’s observations are too small to justify the variations from day to day. As such, we expect the rotation of the nucleus to be the cause of these variances. This is further expanded upon in section 3.2. Figure 3 shows the activity of 62P as determined for a range of aperture radii between 1000 km and 70000 km. For all days in the V and B bands, and one of the days in the R band, we see the activity curves flatten out to a constant with respect to  $\rho$ . This is typically characteristic of a steady state emission, as discussed by Garcia & Gil-Hutton (2021) and references therein. However, under further inspection, at these large apertures, the intensity of the coma approaches the background signal and these observations lack the precision needed to delineate the coma at large  $\rho$ . The reference aperture of  $\rho = 10^4 \text{ km}$  fortunately lies before this region and is well determined. Figure 3 also shows a comparison of the dust rate proxy with archive data for this orbit. 62P was observed by the TRAPPIST robotic telescope on 2023-11-12 (1.36 au), 2024-01-11 (1.28 au), and 2024-02-20 (1.44 au) (Jehin et al. 2023, 2024a,b) with calculations of  $Af\rho$ . Note that each of these measurements also pertains to the standard reference aperture of  $\rho = 10^4 \text{ km}$  and are phase corrected. In figure 3, the data of this study extend the TRAPPIST data-set in characterising the activity evolution post-perihelion.

Date	B	$Af\rho$ [cm]	V	$Af\rho$ [cm]	R	$Af\rho$ [cm]
2024-03-13	$14.55 \pm 0.04$	$42.7 \pm 1.2$	$13.59 \pm 0.01$	$75.9 \pm 0.6$	$13.44 \pm 0.08$	$78 \pm 4$
2024-03-14	$14.19 \pm 0.02$	$58.3 \pm 0.9$	$14.18 \pm 0.10$	$43 \pm 3$	$13.26 \pm 0.10$	$90 \pm 6$
2024-03-15	$14.15 \pm 0.12$	$60 \pm 4.5$	$13.66 \pm 0.05$	$69 \pm 2.4$	$13.78 \pm 0.17$	$55 \pm 6$
2024-03-18	$14.44 \pm 0.15$	$44 \pm 4.5$	$13.88 \pm 0.06$	$54 \pm 2.4$	$13.76 \pm 0.08$	$54 \pm 3$
<b>Weighted Mean</b>	$14.34 \pm 0.16$	$59 \pm 5$	$13.95 \pm 0.23$	$70 \pm 14$	$13.59 \pm 0.22$	$73 \pm 21$

**Table 3. Magnitude and Activity Results:** Magnitude and phase corrected  $Af\rho$  as determined in each photometric filter for each night of observations, all determined with the standard reference aperture radius  $\rho = 10^4$  km. A weighted mean was taken to describe the average behaviour over the course of the four observing nights.

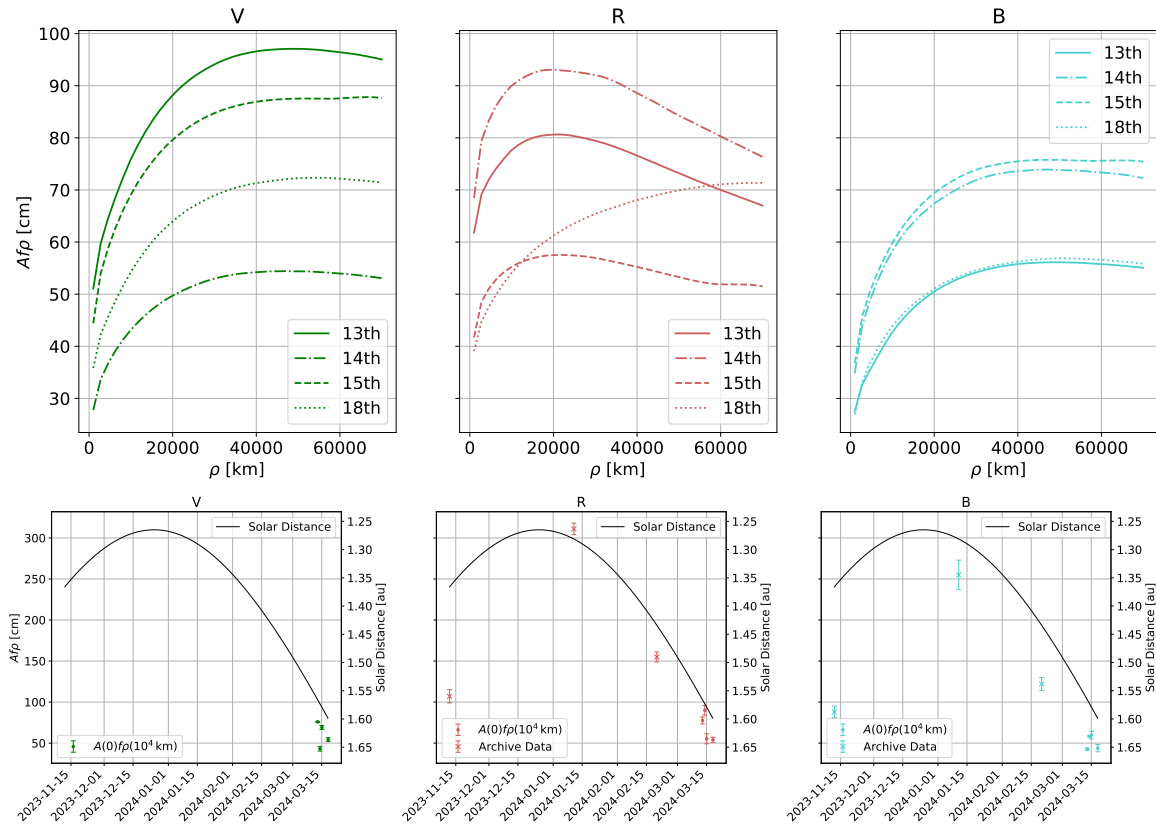


**Figure 3. Activity Evolution:** *Upper panels:*  $Af\rho$ , determined for a range of  $\rho$  between 1000 km and 70000 km and phase corrected to create an  $Af\rho$  profile. The uncertainties on these measurements are not included for clarity, but are  $\mathcal{O}(10\text{ cm})$ . Star removal methods were carried out, yet not fully effective. We see an uncharacteristic increase in  $Af\rho$  values in all bands on the 15th. This corresponds to a background star which could not be reduced further without the creation of significant artifacts in the image. Note that this deviation from the curve is still significantly reduced from the removal methods employed.

*Lower panels:* The  $Af\rho$  values taken at the reference aperture radius  $\rho = 10^4$  km compared with data from TRAPPIST (Jehin et al. 2023, 2024a,b) of previous positions near perihelion. Note that the  $Af\rho$  data was only available with data in comet specialised narrowband filters filters RC (red continuum) and BC (blue continuum) (Farnham et al. 2000). Conversions from magnitudes in these narrowband filters to magnitudes in the broadband Johnson-Cousins filters don't exist, however, as the narrowband filters are centred near the peak of the broadband continuum, for the purposes of comparing activity measurements we assume them to be equivalent. Note that the data in the V filter could not be compared as there were no equivalent data available. The black line overplotted is the heliocentric distance (note the flipped axis orientation). We do not expect the data to follow this curve, however, the general behaviour gives overall context to the environment.

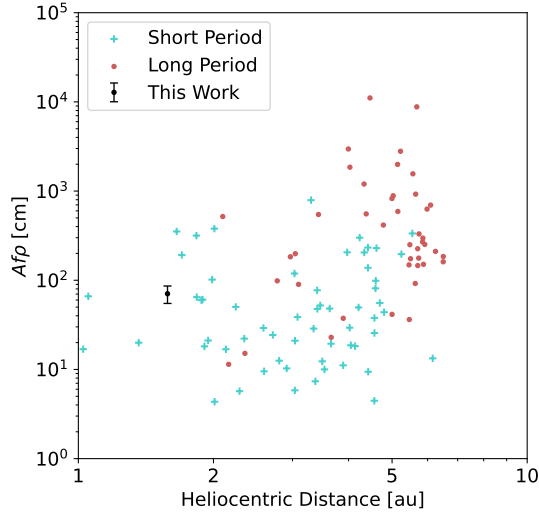


**Figure 4. Activity against Heliocentric Distance:** Average R band  $Af\rho$  for 62P with the context of other short period (blue pluses) and long period (red dots) comets with data from Garcia & Gil-Hutton (2021) and references therein. We see that the observations from this work agree well with that from other short period comets. Note that activity of a comet will change along its orbit and as such point values are somewhat arbitrary, however, the general behaviour is still important for comparison. We expect comets to typically trace closed loops on this plot as they move along a full period of their orbit.

The mean R band activity calculated in table 3 was plotted against the average heliocentric distance over the course of the observations, and compared to other short and long period comets in figure 4 with data from Garcia & Gil-Hutton (2021) and references therein. Exact values are less relevant in this plot as we expect each short period comet to trace out a closed loop on this plot over the course of its orbit. Generally, the activity of 62P compares well to other short period comets and has characteristic dust production rates.

### 3.2. Dust Colour

For each night of observations, the colour indices  $B-V$  and  $V-R$  were determined from the magnitudes calculated in table 3 and recorded in table 4. Again, the weighted mean across all four days was taken. These data along with their mean were plotted in figure 5 as  $V-R$  against  $B-V$ . Dashed black lines overlotted correspond to the sun colours (Holmberg et al. 2006). We observe that the comet is anomalously close to, if not bluer than the sun colour in both  $B-V$  and  $V-R$ , we expect dust colours of any short period comet to be considerably redder than the sun (Bauer et al. 2022; Meech et al. 2009; Ivanova et al. 2014). However, ac-

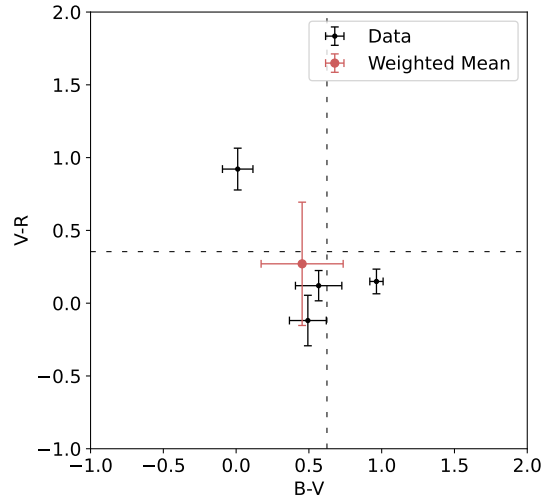


**Figure 5. Comet/Sun Colour Comparison:** Colour index values from table 4 plotted. The sun colours are marked by dashed black lines (Holmberg et al. 2006). We see a lot of variation over the four observations but the mean behaviour (as marked by the red point) appears similar to the sun and somewhat bluer. A considerable difference from the expected colour distribution of short period (and long period) comets as shown by Bauer et al. (2022).

curate determination of comet dust colours requires photometry with filters free from gas emission (Meech et al. 2009). When near the sun, comets typically have strong emission from CN, C<sub>3</sub>, C<sub>2</sub>, and NH<sub>2</sub> in the B filter, and emission from C<sub>2</sub>, and NH<sub>2</sub> in the V filter, with only minor emission in R from NH<sub>2</sub> and [OI] (Meech et al. 2009). The strength of these emissions varies with  $r^{-2}$  (Meech et al. 2009), and as such, the dust colour of 62P was most likely affected by strong gas emissions (Ivanova et al. 2014). This was confirmed with prior observations from TRAPPIST (Jehin et al. 2023, 2024a,b) which at perihelion detected OH, NH, CN, C<sub>2</sub>, and C<sub>3</sub>. Table 5 contains the molecule production rates determined for the months surrounding perihelion.

The day to day variations in the measured colour and reddening were uncharacteristically dramatic over a short term period. The reddening variations as determined for each observation are shown in figure 6. These variations are outside the region of uncertainty from the mean to warrant changes due to evolution (which is not an uncommon finding (Voitko et al. 2022; Ivanova et al. 2017; Weiler et al. 2003), and hence, given the near constant phase angle and other observing conditions (Zubko et al. 2014), must occur by some other means (Voitko et al. 2022; Ivanova et al. 2017). Two potential scenarios presented in the literature could provide reasoning for this result. The first of which suggests that due to

Date	B-V	V-R	Reddening (B-V)	Reddening (V-R)
2024-03-13	$0.96 \pm 0.05$	$0.15 \pm 0.08$	$7.3 \pm 5$	$0.2 \pm 5$
2024-03-14	$0 \pm 0.1$	$0.92 \pm 0.14$	$-2.5 \pm 5$	$10 \pm 2$
2024-03-15	$0.5 \pm 0.13$	$-0.12 \pm 0.17$	$1.5 \pm 0.9$	$-1.9 \pm 0.9$
2024-03-18	$0.57 \pm 0.16$	$0.1 \pm 0.1$	$2.2 \pm 1.3$	$0 \pm 0.6$
Weighted Mean	$0.45 \pm 0.3$	$0.3 \pm 0.4$	$0.9 \pm 2.7$	$2 \pm 4$

**Table 4. Dust Colours:** Dust colours measured with  $B - V$  and  $V - R$  determined from magnitudes in table 3, along with reddening (% change in the continuum strength per 1000 Å) between B and V, and V and R, determined from activity data in table 3. Again a weighted mean was taken of the colour indices to better represent the average behaviour during the course of the four observing nights. Reddening values were only determined for mean activities. We see significant variation in both colour indices and reddening. This is most likely due to rotations in the comet and a heterogeneous composition.

Date	Q(OH) [ $10^{27} \text{ s}^{-1}$ ]	Q(NH) [ $10^{25} \text{ s}^{-1}$ ]	Q(CN) [ $10^{25} \text{ s}^{-1}$ ]	Q(C <sub>2</sub> ) [ $10^{25} \text{ s}^{-1}$ ]	Q(C <sub>3</sub> ) [ $10^{24} \text{ s}^{-1}$ ]
2023-11-12	$(3.93 \pm 0.79)$	-	$(1.21 \pm 0.04)$	$(1.34 \pm 0.06)$	$(2.39 \pm 0.18)$
2024-01-11	$(9.06 \pm 0.98)$	$(7.53 \pm 0.64)$	$(3.15 \pm 0.12)$	$(3.34 \pm 0.08)$	$(6.11 \pm 0.25)$
2024-02-20	$(2.68 \pm 0.46)$	-	$(1.37 \pm 0.07)$	$(1.37 \pm 0.10)$	$(2.72 \pm 0.18)$

**Table 5. Molecule Production:** Trappist molecule production data from key points surrounding the perihelion - note the different scalings for each molecule. Rows containing a dash mark molecules not detected for that observation. The second observation is placed two weeks after perihelion, we see molecule production increases and subsequently drops to levels similar to observations prior to perihelion.

outbursts in activity, the dust colour of a comet can change rapidly. However as presented by [Voitko et al. \(2022\)](#), such outbursts in activity would need to coincide with a similar increase in comet brightness. We do observe this in the B filter data, however we also see a large decrease in V band magnitude. The second and more likely scenario is that the comet is chemically heterogeneous ([Ivanova et al. 2017](#)) and as such, rotations of the nucleus will reveal areas on the nucleus of different composition yielding variations in the colour.

### 3.3. Nucleus Radius

The nucleus magnitude and total magnitude were determined through the coma correction method and, by taking  $m_{\odot} = -27.1$  ([Holmberg et al. 2006](#)) in the R band, an upper limit to the radius of the nucleus was found to be  $r_{\text{nucleus}} \leq 5.48 \text{ km}$  for an assumed albedo  $A = 0.04$ . Figure 7 shows a radius curve for albedo values from  $A = 0.02$  - the lowest measured albedo ([A’Hearn et al. 1989](#)) - through  $A = 0.04$  - the ‘standard’ albedo value ([Mazzotta Epifani et al. 2007](#)) - up to more unlikely high albedos of  $A = 0.13$  ([Bus et al. 1989](#); [Cruikshank & Brown 1983](#)).

As 62P is active and has a large coma, it is difficult to measure accurately its nucleus. In fact, this measurement is a large overestimate despite the measures taken to exclude the coma contamination. Observations of 62P at 4.72 au in 2006 revealed an accurate measure-

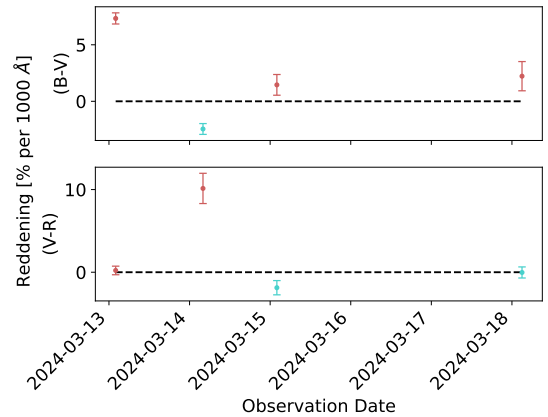


**Figure 6. Colour Variations:** Dramatic reddening variations observed from day to day. The dashed black line corresponds to a continuum slope of 0%, days where a positive slope was observed were coloured red, and days where a negative slope was observed were coloured blue.

ment of the nucleus radius,  $r_{\text{nucleus}} = (0.59 \pm 0.09) \text{ km}$  ([Fernández et al. 2013](#)). However, this is not unusual for such measurements of active comets. Take observations of 74P/Smirnova-Chernykh by [Lowry & Fitzsimmons \(2001\)](#) for example, which record upper limits of  $r_{\text{nucleus}} \leq 12.7 \text{ km}$ , compared to later observations by [Tancredi et al. \(2006\)](#) of the same comet, finding  $r_{\text{nucleus}} = 3.17 \text{ km}$  ([Mazzotta Epifani et al. 2007](#)).

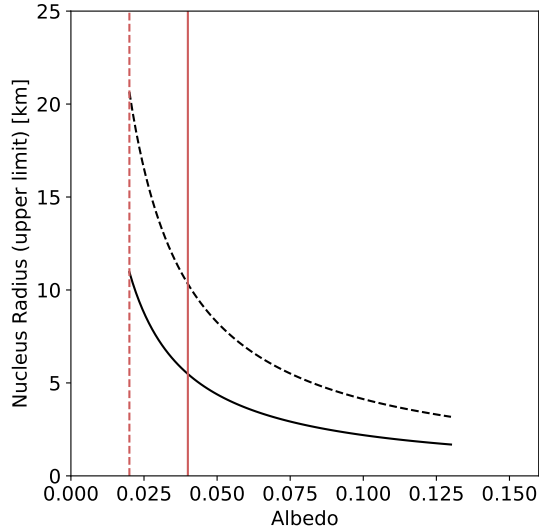


**Figure 7. Radius Curve:** The radius curve for 62P with albedo values ranging from  $A = 0.02$  (dashed red vertical line) to  $A = 0.13$ , with the assumed albedo of  $A = 0.04$  marked with a solid red vertical line. The solid black curve corresponds to the calculation with the coma contamination considered, whereas the dashed black curve corresponds to the total magnitude at the same aperture.

#### 4. CONCLUSIONS

We presented new photometric observations of short period comet 62P/Tsuchinshan 1. From these observations, the phase corrected dust rate proxy was determined for  $\rho = 10^4$  km, with an average R band  $Af\rho = (73 \pm 21)$  cm at a heliocentric distance of  $R_h = 1.58$  au. The measurements of this work extend prior measurements of  $Af\rho$  earlier in the orbit, which agree well with each other. The activity measurements were also compared in the context of a large collection of data for short and long period comets with the  $Af\rho$  value of 62P comparing well with other short period comets at similar heliocentric distances. Dust colour was also determined with average colour indices  $B - V = 0.45 \pm 0.3$  and  $V - R = 0.3 \pm 0.4$  with reddening =  $(0.9 \pm 2.7)$  % per  $1000 \text{ \AA}$  between the B and V bands, and reddening =  $(2 \pm 4)$  % per  $1000 \text{ \AA}$  between the V

and R bands. These comet colours are bluer than the sun, and hence the presence of gas emission was inferred. This is consistent with spectroscopic measurements of 62P which detect several species in large abundances. The observations of 62P showed dramatic variations on a short time scale. As these variations were not accompanied by a significant increase in comet brightness (characteristic of outburst activity), it was inferred that 62P must be chemically heterogeneous, and rotations of the nucleus are driving these variations. An upper estimate of the radius of the nucleus was determined to be  $r_{\text{nucleus}} \leq 5.48$  km, which agrees with past measurements.

#### DATA AVAILABILITY STATEMENT

All of the code used to create the figures and calculations in this paper are available online via Github (<https://github.com/daraghollman/Comet62P-Tsuchinshan>). All raw data and derived data products are also available via Zenodo at DOI: (10.5281/zenodo.11072638).

#### ACKNOWLEDGMENTS

This work was carried out with the use of Python 3.11.8 (<https://www.python.org/downloads/release/python-3118/>) and notable packages ASTROPY, PHOTUTILS, SCIPY, NUMPY, MATPLOTLIB, ASTROQUERY, and UNCERTAINTIES. I would like to thank my girlfriend Sadbh (who so desperately wanted to name this comet) and my family for their endless support throughout this work and my entire final year of my undergraduate degree, and mostly for always having a free minute to hear me talk (or rant) about an icy rock quite frankly way too far away to warrant their interest. I would also like to thank my supervisor Dr. Antonio Martin-Carrillo, mostly for his help and dedication with this study (despite having a million and one other things he should've been working on), but also for the countless games of table tennis we played whilst at Calar Alto which he so graciously lost; they were thoroughly enjoyable.

#### REFERENCES

- A'Hearn, M. F., Campins, H., Schleicher, D. G., & Millis, R. L. 1989, ApJ, 347, 1155, doi: [10.1086/168204](https://doi.org/10.1086/168204)
- A'Hearn, M. F., Schleicher, D. G., Millis, R. L., Feldman, P. D., & Thompson, D. T. 1984, AJ, 89, 579, doi: [10.1086/113552](https://doi.org/10.1086/113552)
- Astropy Collaboration, Price-Whelan, A. M., Lim, P. L., et al. 2022, ApJ, 935, 167, doi: [10.3847/1538-4357/ac7c74](https://doi.org/10.3847/1538-4357/ac7c74)
- Bauer, J. M., Fernández, Y. R., Protopapa, S., & Woodney, L. M. 2022, arXiv e-prints, arXiv:2210.09400, doi: [10.48550/arXiv.2210.09400](https://doi.org/10.48550/arXiv.2210.09400)

- Bradley, L., Sipőcz, B., Robitaille, T., et al. 2023, *astropy/photutils*: 1.10.0, 1.10.0, Zenodo, doi: [10.5281/zenodo.1035865](https://doi.org/10.5281/zenodo.1035865)
- Bus, S. J., Bowell, E., Harris, A. W., & Hewitt, A. V. 1989, *Icarus*, 77, 223, doi: [10.1016/0019-1035\(89\)90087-0](https://doi.org/10.1016/0019-1035(89)90087-0)
- Cochran, A. L., Levasseur-Regourd, A.-C., Cordiner, M., et al. 2015, *SSRv*, 197, 9, doi: [10.1007/s11214-015-0183-6](https://doi.org/10.1007/s11214-015-0183-6)
- Cruikshank, D. P., & Brown, R. H. 1983, *Icarus*, 56, 377, doi: [10.1016/0019-1035\(83\)90158-6](https://doi.org/10.1016/0019-1035(83)90158-6)
- Farnham, T. L., Schleicher, D. G., & A’Hearn, M. F. 2000, *Icarus*, 147, 180, doi: [10.1006/icar.2000.6420](https://doi.org/10.1006/icar.2000.6420)
- Fernández, Y. R., Kelley, M. S., Lamy, P. L., et al. 2013, *Icarus*, 226, 1138, doi: [10.1016/j.icarus.2013.07.021](https://doi.org/10.1016/j.icarus.2013.07.021)
- Garcia, R. S., & Gil-Hutton, R. 2021, *Planet. Space Sci.*, 206, 105308, doi: [10.1016/j.pss.2021.105308](https://doi.org/10.1016/j.pss.2021.105308)
- Giorgini, J. D., Yeomans, D. K., Chamberlin, A. B., et al. 1996, in *AAS/Division for Planetary Sciences Meeting Abstracts*, Vol. 28, AAS/Division for Planetary Sciences Meeting Abstracts #28, 25.04
- Henden, A. A., Templeton, M., Terrell, D., et al. 2016, *VizieR Online Data Catalog: AAVSO Photometric All Sky Survey (APASS) DR9 (Henden+, 2016)*, *VizieR On-line Data Catalog: II/336*. Originally published in: 2015AAS...22533616H
- Holmberg, J., Flynn, C., & Portinari, L. 2006, *MNRAS*, 367, 449, doi: [10.1111/j.1365-2966.2005.09832.x](https://doi.org/10.1111/j.1365-2966.2005.09832.x)
- Ivanova, O., Borysenko, S., & Golovin, A. 2014, *Icarus*, 227, 202, doi: [10.1016/j.icarus.2013.08.026](https://doi.org/10.1016/j.icarus.2013.08.026)
- Ivanova, O., Zubko, E., Videen, G., et al. 2017, *MNRAS*, 469, 2695, doi: [10.1093/mnras/stx1004](https://doi.org/10.1093/mnras/stx1004)
- Jehin, E., Donckt, M. V., Hmiddouch, S., & Manfroid, J. 2023, *The Astronomer’s Telegram*, 16338, 1
- . 2024a, *The Astronomer’s Telegram*, 16408, 1
- . 2024b, *The Astronomer’s Telegram*, 16338, 1
- Jewitt, D. 1991, *Cometary Photometry*, ed. R. L. Newburn, M. Neugebauer, & J. Rahe (Dordrecht: Springer Netherlands), 19–65, doi: [10.1007/978-94-011-3378-4\\_2](https://doi.org/10.1007/978-94-011-3378-4_2)
- Jordi, K., Grebel, E. K., & Ammon, K. 2006, *A&A*, 460, 339, doi: [10.1051/0004-6361:20066082](https://doi.org/10.1051/0004-6361:20066082)
- Kolokolova, L., Hanner, M. S., Levasseur-Regourd, A. C., & Gustafson, B. Å. S. 2004, in *Comets II*, ed. M. C. Festou, H. U. Keller, & H. A. Weaver, 577
- Korsun, P. P., & Chörny, G. F. 2003, *A&A*, 410, 1029, doi: [10.1051/0004-6361:20031116](https://doi.org/10.1051/0004-6361:20031116)
- Lamy, P. L., Toth, I., Fernandez, Y. R., & Weaver, H. A. 2004, in *Comets II*, ed. M. C. Festou, H. U. Keller, & H. A. Weaver, 223
- Lara, L. M., Licandro, J., Oscoz, A., & Motta, V. 2003, *A&A*, 399, 763, doi: [10.1051/0004-6361:20021720](https://doi.org/10.1051/0004-6361:20021720)
- Li, J., Shi, J., & Ma, Y. 2023, *MNRAS*, 518, 3192, doi: [10.1093/mnras/stac3269](https://doi.org/10.1093/mnras/stac3269)
- Lowry, S. C., & Fitzsimmons, A. 2001, *A&A*, 365, 204, doi: [10.1051/0004-6361:20000180](https://doi.org/10.1051/0004-6361:20000180)
- Mazzotta Epifani, E., Dall’Ora, M., di Fabrizio, L., et al. 2010, *A&A*, 513, A33, doi: [10.1051/0004-6361/200913535](https://doi.org/10.1051/0004-6361/200913535)
- Mazzotta Epifani, E., Palumbo, P., Capria, M. T., et al. 2007, *MNRAS*, 381, 713, doi: [10.1111/j.1365-2966.2007.12181.x](https://doi.org/10.1111/j.1365-2966.2007.12181.x)
- Meech, K. J., Pittichová, J., Bar-Nun, A., et al. 2009, *Icarus*, 201, 719, doi: [10.1016/j.icarus.2008.12.045](https://doi.org/10.1016/j.icarus.2008.12.045)
- Mommert, M., Kelley, M., de Val-Borro, M., et al. 2019, *The Journal of Open Source Software*, 4, 1426, doi: [10.21105/joss.01426](https://doi.org/10.21105/joss.01426)
- O’Ceallaigh, D. P., Fitzsimmons, A., & Williams, I. P. 1995, *A&A*, 297, L17
- Schleicher, D. 2010, *Composite Dust Phase Function for Comets*, <https://asteroid.lowell.edu/comet/dustphase/>
- Tancredi, G., Fernández, J. A., Rickman, H., & Licandro, J. 2006, *Icarus*, 182, 527, doi: [10.1016/j.icarus.2006.01.007](https://doi.org/10.1016/j.icarus.2006.01.007)
- Voitko, A., Zubko, E., Ivanova, O., et al. 2022, *Icarus*, 388, 115236, doi: [10.1016/j.icarus.2022.115236](https://doi.org/10.1016/j.icarus.2022.115236)
- Weiler, M., Rauer, H., Knollenberg, J., Jorda, L., & Helbert, J. 2003, *A&A*, 403, 313, doi: [10.1051/0004-6361:20030289](https://doi.org/10.1051/0004-6361:20030289)
- Zubko, E., Muinonen, K., Videen, G., & Kiselev, N. N. 2014, *MNRAS*, 440, 2928, doi: [10.1093/mnras/stu480](https://doi.org/10.1093/mnras/stu480)

## APPENDIX

## A. STACKED IMAGES FOR ALL OBSERVING DATES

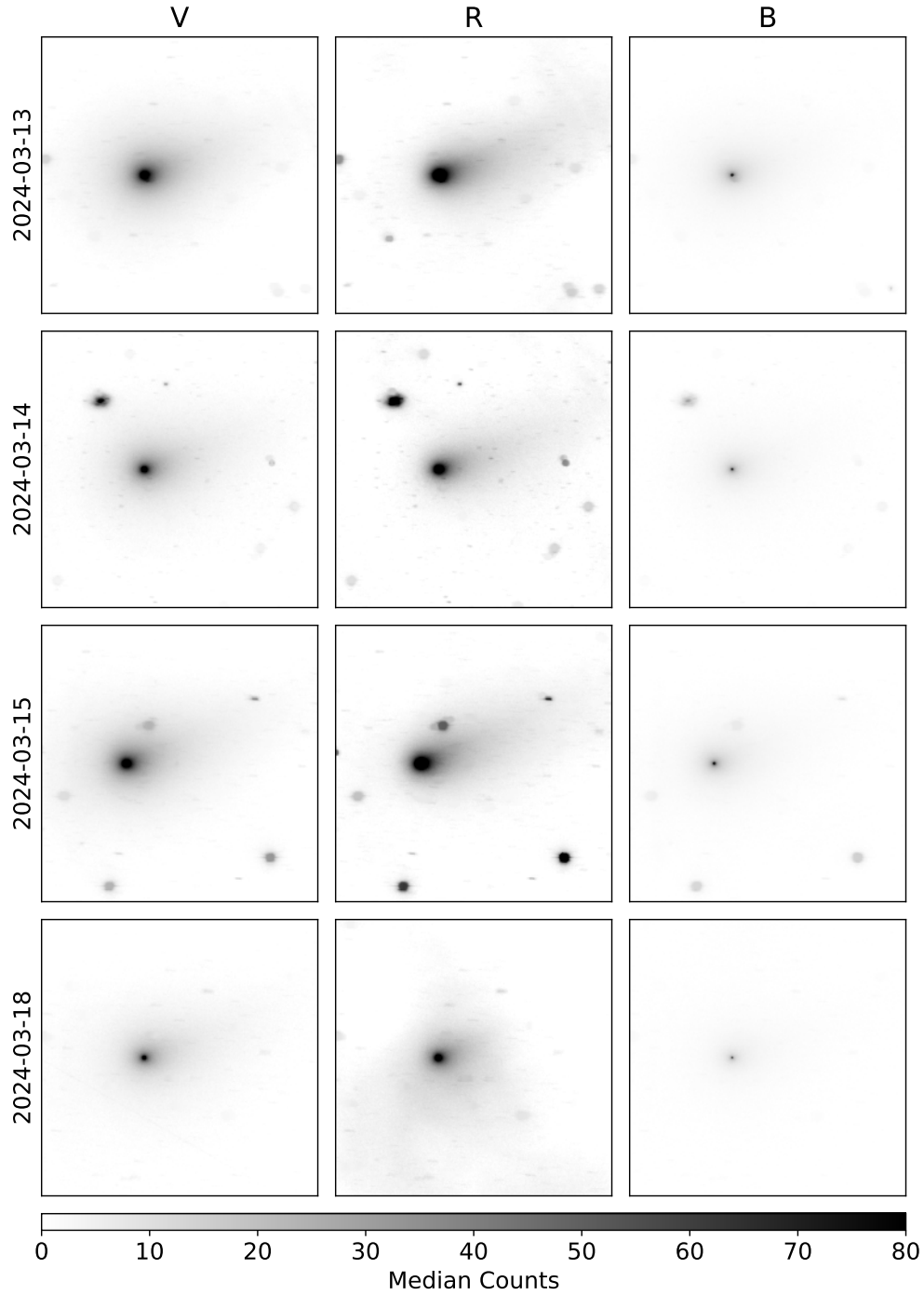


**Figure A.1. All Stacked Images:** Stacked observations for each night as in figure 1. Note apparent changes in brightness are dominated by observing conditions and not by changes in the comet.

## B. CHOSING AN APPROPRIATE APERTURE TO DETERMINE COMA CONTAMINATION

When finding the coma correction to the nucleus magnitude, some detail is required to fully explain the choice of reference aperture at which to evaluate equation 3. The surface brightness profile was determined through photometry of small concentric annuli - ring width  $0.6''$  - to an extent of  $80''$ , limited by the influence of nearby field stars. Figure B.2 shows the surface brightness profile within  $10''$  of the comet. We see the contribution from the nucleus drop quickly to a fluctuating but constant surface brightness, corresponding to the coma. For clarity, this figure was only plotted to  $10''$ , however these fluctuations around a constant surface brightness were observed out to the full extent of  $80''$ .

The mean coma surface brightness was determined to be  $(19.364 \pm 0.002)$  mag/arcsec<sup>2</sup> between  $2''$  and  $80''$ . The reference aperture at which to evaluate equation 3 was determined to be the point closest to the nucleus signal, yet still definitively representative of the coma signal. This was chosen to be where the surface brightness profile approached three standard deviations above the mean coma surface brightness to ensure an upper limit. This reference aperture was determined to be at  $1.71''$ , as denoted by the vertical line in figure B.2. It is important to note, that the amplitude of these fluctuations was directly tied to the choice of annulus width. Larger annuli sample over a larger region of sky and better represent the azimuthally averaged signal and hence would reduce the amplitude of fluctuations, however due to the small extent of the nucleus signal, increasing the width of the annuli resulted in not being able to differentiate the nucleus signal.

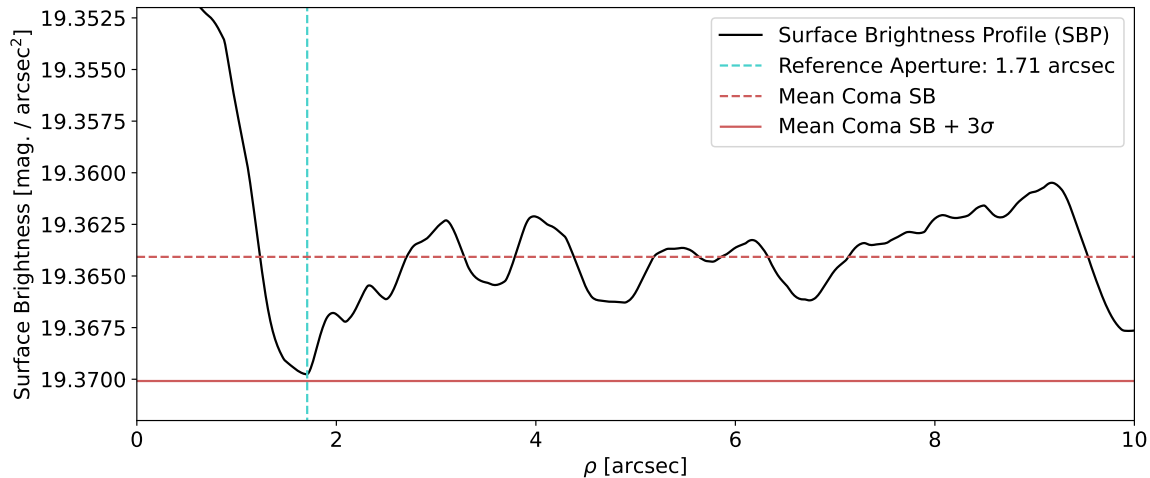


**Figure B.2. Surface Brightness Profile:** The surface brightness profile from the centre of the comet out to  $10''$ . We see a clear drop off from where the point spread function of the nucleus meets the coma signal. Note the similarities to figure 2. The mean of the surrounding coma signal was taken, and the reference aperture at which to perform coma contamination calculations was determined to be where the surface brightness was closest to three standard deviations above the mean of the coma signal. The fluctuations in the coma surface brightness are due to the use of a small annulus size, however, larger annuli cannot be used without sacrificing the necessary precision require to highlight the difference between the surface brightness of the nucleus and of the coma at small  $\rho$ .